Planar polarized force propagation integrates cell behavior and tissue morphogenesis during convergent extension

Shinuo Weng[1], Robert J. Huebner[1], Caitlin C. Devitt[1], Bill M. Nyaoga[1], José R. Alvarado[2], John B. Wallingford[1,*]

1. Department of Molecular Biosciences, University of Texas at Austin, Austin, TX 78712, USA
2. Department of Physics, University of Texas at Austin, Austin, TX 78712, USA

*Correspondence to:

John Wallingford
Patterson Labs
2401 Speedway
Austin, Texas
78712
Wallingford@austin.utexas.edu
512-232-2784

Abstract:

Convergent extension (CE) is an evolutionarily conserved developmental process whereby polarized collective cell movements drive the elongation of tissues or organs, and defects in CE are associated with multiple human birth defects. Here, we combined embryology with cell biology and newly developed biomechanical tools to interrogate the link between cell behavior and tissue-scale CE. We found that unique patterns of polarized cortex tension are required to resolve individual cell intercalation events, and this in turn maintains normal cell packing configurations that favor the planar propagation of the cellular forces across the tissue, and thus normal CE. Our data suggest that planar polarized force propagation plays a critical role in the propagation of cell behaviors via cellular mechanoreciprocity, underpinning the propagation of tissue-scale CE.

Introduction:

Convergent extension (CE) is an evolutionarily conserved morphogenetic process that not only elongates the body axis of almost all animals but also of several organ systems, including kidney and heart (Kidokoro, et al., 2018; Lienkamp, et al., 2012; Tada and Heisenberg, 2012; Keller, 2002). Genes controlling CE are also linked to several birth defects, including neural tube defects and skeletal dysplasias (Butler and Wallingford, 2017; Wallingford, et al., 2013). Convergence is achieved via a series of steps, including the establishment of planar cell polarity, polarized actomyosin activity, and repeated mediolaterally-directed cell intercalations that effect tissue elongation int eh perpendicular, anteroposterior direction (Sutherland, et al., 2020). Thus, CE is an emergent process that requires elaborate coordination between events across different length and time scales.

Mechanical signals, at both long-range and short-range are a key mechanism for integration across length scales (Goodwin and Nelson, 2021; Maroudas-Sacks and Keren, 2021; Abuwarda and Pathak, 2020), so CE is associated with several dynamic mechanical cues. At the macroscale, mechanical interactions between tissues play critical roles in CE. Examples include the posterior mid-gut invagination pulling on the germband to induce polarized cell shape change and promote CE during *Drosophila* germband extension (Yu and Fernandez-Gonzalez, 2016; Collinet, et al., 2015), as well as migrating head mesoderm pulling on the subsequent notochord during *Xenopus* notochord CE (Hara, et al., 2013). Meanwhile, tissues undergoing CE also stiffen progressively (Zhou, et al., 2009), which is essential to overcome the physical resistance from the surrounding tissue (Huebner, et al., 2022). At the microscale, the integration of actin and myosin-based polarized pushing and pulling at cell-cell interfaces drives polarized cell intercalation (Weng, et al., 2022; Shindo, 2018). Interestingly, actin and myosin activities are also required for tissue stiffening (Zhou, et al., 2009). Together, these bottom-up effects and top-down effects suggest multiscale mechanical feedback is required for effective CE.

Linkage of cells by cadherin-based adhesion complexes are critical for morphogenetic processes, including CE (Huebner, et al., 2022; Arslan, et al., 2021; Levayer and Lecuit, 2013; Niessen, et al., 2011), and such adhesions are known to be mechanosensitive (Pannekoek, et al., 2019; Ladoux and Mege, 2017). Recently, we identified a strong *in vivo* interaction between cadherin and Arvcf, a poorly characterized catenin required for *Xenopus* notochord CE

(Huebner, et al., 2022; Fang, et al., 2004; Paulson, et al., 2000). Interestingly, we found that Arvcf is required for normal tissue-scalle force generation during Ce, but unlike most known regulators of CE, Arvcf is largely dispensable for polarized cell intercalation (Huebner, et al., 2022). This finding provided us a unique example where cell intercalations do not guarantee a successful tissue scale CE, so we used this model to explore the linkage of cell- and tissue scale forced during CE.

In this study, we explore the mechanical mechanisms by which cell intercalation behaviors are linked to tissue-scale CE of the *Xenopus* notochord. By combining embryology and cell biology and developing novel tools for non-invasive assessment of cell cortex tension, we found that a unique pattern of the ML-aligned junction tensions was required to fully resolve individual cell intercalation events; and this process maintains normal cell packing configurations and allows the ML-aligned cellular forces to propagate in the direction of tissue elongation. By contrast, in the absence of Arvcf, ML-aligned junction tensions were reduced, and cells took on aberrant packing configurations that effectively blocked the propagation of both cellular forces and tissue-scale CE. Together, these data are significant for providing new biomechanical and cell biological insights into a multiscale morphogenetic process that is implicated in human neural tube defects and skeletal dysplasia.

Results:

CE propagation along the anteroposterior axis is required for embryonic elongation

To understand the link between tissue scale CE and the underlying cell behaviors, we started by further characterizing the effect of Arvcf loss on the morphology of the developing notochord. Previous work has reported that CE cell behaviors initiate in the anterior notochord and propagate towards the posterior (Shih and Keller, 1992). Accordingly*, in situ* hybridization for the notochord-specific marker *Xnot* (von Dassow, et al., 1993) in *en face* projections was trapezoidal and narrower at the anterior in normal embryos at mid-gastrulation (NF stage 11.5; **Fig. 1A**, left). The notochord then quickly reorganized into a slim rectangle by early neurulation (NF stage 14; **Fig. 1A**, right), leaving no difference on the tissue width at its anterior and posterior (**Fig. 1C**, blue).

Loss of Arvcf disrupts CE *in vivo* leading to a shorter and wider notochord (Huebner, et al., 2022), but interestingly, *in situ* hybridization revealed that this defect was not uniform along the AP axis. At mid-gastrulation, the notochord in Arvcf-KD embryos was trapezoidal, similar to a WT tissue; however, at early neurulation, the notochord remained narrower anteriorly and much wider at the posterior (**Fig.1B; 1C**, orange). This result suggests the possibility that the tissue-level defect resulting from Arvcf depletion stems from a failure of CE propagation.

To understand this phenotype, we excised and cultured the dorsal mesoderm tissue *ex vivo* (Keller explant), with which cell behaviors and tissue shape change can be tracked over time. WT explants displayed an obvious AP extension and underwent tissue-wide convergence progressively along the AP axis (**Fig. 1D**). We measured the amount of AP extension, as well as ML convergence at three difference positions along the AP axis as illustrated in **Fig 1F**. The data further confirmed tissue elongation and even convergence along the AP axis (**Fig. 1G, H**, blue), consistent with the phenotypes in embryos (**Fig. 1A**). By contrast, extension in Arvcf KD explants was mostly eliminated (**Fig. 1E, G**), and convergence was only consistently observed at their anterior (**Fig. 1E**). Quantification of the ML convergence also revealed that there was no significant reduction of convergence at the most anterior end, but more toward posterior, the reduction of convergence was exaggerated (**Fig. 1H**), similar to the embryonic phenotype (**Fig. 1B**). Moreover, we consistently observed multiple local convergences in the middle-to-posterior regions of explants (**Fig. 1e'**, black arrows), which were surrounded by regions with limited convergence (**Fig. 1e'**, gray arrowheads). These data demonstrate that loss of Arvcf results in impaired propagation of convergence along the AP axis, leading to a tissue-wide CE defect.

Loss of Arvcf leads to aberrant cell packing configurations

We next sought to understand the cell behaviors underlying the tissue-wide CE propagation defect elicited by Arvcf depletion. CE is accomplished by the shortening of so-called v-junctions, which link anteroposterior neighboring cells (**Fig. 2A**, light gray), but the rate of v-junction shortening was only modestly affected by Arvcf KD (Weng, et al., 2022). A second commonly used parameter, mediolateral cell elongation, was also unchanged (**Fig. S1**). These findings suggest that the CE propagation defect may be caused by alteration of higher order features beyond the scale of single, individual cells. Consistent with this idea, we noticed an intriguing difference in cell packing configurations between WT and Arvcf KD explants.

In WT explants, junctions separating mediolateral cells (i.e., t-junctions (**Fig. 2A**, dark gray) were generally tilted relative to the apposed v-junctions (**Fig. 2b'**), and only a small portion of t-junctions were perpendicular to the connected v-junctions (i.e. were strongly aligned in the AP axis; referred to as "AP-aligned t-junctions"; **Fig. 2B**, hollow arrowheads). To quantify this pattern, we measured the smaller angle between t- and connected v-junctions for each cell (referred to as "tricellular angles", **Fig. 2b'**). We found that tricellular angles in WT explants peaked around 40°, consistent with the general tilt of t-junctions described above (**Fig. 2D**, blue).

By contrast, Arvcf KD explants had significantly more AP-aligned t-junctions (**Fig. 2C**, hollow arrowheads). The tricellular angle measurement further revealed a dominant peak formed around 90°, corresponding to the perpendicular, AP-aligned t-junctions (**Fig.2D**, orange). This unexpected and significant change in the orientation of t-junctions suggests a link between aberrant cell packing configurations and the tissue-scale CE defect.

Normal cell packing requires t-junction rotation

T-junctions emerge after v-junction shortening is completed to bring the mediolateral cells into contact (**Fig. 2A**). However, despite recent work on t-junction formation in *Drosophila* (Yu and Fernandez-Gonzalez, 2016; Collinet, et al., 2015), how t-junctions form and remodel in other settings remains largely undefined. We therefore used live imaging of a membrane marker to characterize the dynamics of t-junction formation in the *Xenopus* notochord.

We identified a two-step process. First the nascent t-junction extended in the direction perpendicular to the shortened v-junction. Second, the t-junction rotated towards either left or right (**Fig. 2E-F**). Neither extension nor rotation was eliminated by the loss of Arvcf (**Fig. 2G**), but the dynamics of the process were altered. Specifically, loss of Arvcf significantly prolonged the extension phase (**Fig. 2H**) but did not change the extension rate (**Fig. 2I**). Moreover, the rate of rotation was also dramatically reduced (**Fig. 2J**), suggesting that timely rotation is required to drive the transition from extension to rotation during t-junction formation. Together, these data suggest that the increased number of AP-aligned t-junctions and the aberrant cell packing configuration observed in Arvcf deficient tissues result from impaired t-junction rotation.

Image-based non-invasive method to assess junctional tension *in vivo*

We next sought to understand the biomechanical basis for t-junction rotation. In *Drosophila* epithelial cells, t-junction growth is driven by pulling forces originating from apical constriction in connected cells but not by junctional tension (Yu and Fernandez-Gonzalez, 2016; Collinet, et al., 2015). Thus, we asked if new t-junction formation in our system was also driven by forces from the surrounding cells, specifically the junctional tension of connected v-junctions.

To this end, we developed a new image-based, non-invasive method named Tension by Transverse Fluctuation ("TFlux") that allows spatially and temporally resolved quantification of forces at cell-cell interfaces *in vivo* (see **Method** for the details; **Fig. S2**). In previous work, we had found that transverse fluctuation of vertices binding V-junctions could be used to report local mechanics (Huebner, et al., 2021). Here, we extend that work by performing similar analysis of all pixels along a cell-cell junction and treating the overall junctions as a semiflexible filament under tension such that its transverse fluctuation, U is inversely correlated to the tension (illustrated in **Fig. 3A**). Intuitively, higher junctional tensions result in less transverse fluctuation and vice versa. For quantification, we used the reciprocal of the mean square transverse fluctuation (i.e., $1/\langle|U|^2\rangle$) as a proxy for the junctional tension (Alvarado and Koenderink, 2014).

As a positive control for this method, we first compared tension on v- and t-junctions in WT explants. Previously, we performed laser cutting experiments and found faster junction recoil and higher tension on v-junctions (Shindo and Wallingford, 2014). Consistent with those data, TFlux revealed that v-junctions displayed lower transverse fluctuation -and thus greater tension- than did t-junctions (**Fig. 3B&C**, blue). Moreover, we have previously reported that the amplitude of actomyosin pulses is dramatically reduced in Arvcf-depleted v-junctions (Huebner, et al., 2022), and consistent with that result, we found that such junctions also display dramatically reduced tension, as indicated by increased transverse fluctuation in TFlux (**Fig. 3C**). Together, these data indicate that TFlux is reliable under different well-controlled conditions.

T-junction rotation requires differential high tension on the connected v-junctions

Our new method allowed us to directly correlate the dynamics of t-junction extension and rotation with tensions of the neighboring junctions (**Fig. 3D, E**). We first examined the effect of average v-junctional tension on t-junction formation. Similar to *Drosophila* epithelial cells (Collinet, et al., 2015), t-junction extension rate in *Xenopus* notochord had little to no correlation to the average tension on the connected v-junctions in either WT or Arvcf deficient explants (**Fig. S3A**). This was consistent with our finding that Arvcf depletion reduced v-junction tension but had no effect on the t-junction extension rate (**Fig. 2I**, **3C**).

Surprisingly, the correlation between the average tension and the t-junction rotation rate was also weak (**Fig. S3B**). Instead, we found it was planar polarization of these tensions that determined rotation, such that diagonally connected regions of high tension directed rotation. That is, new t-junctions in WT explants rotated clockwise when tensions on the upper right and lower left v-junctions were higher than tensions on the other diagonal pair, and vice versa (**Fig. 3E, F)**.

To quantify this result, we introduced a new term $\Delta 1/\langle |U|^2 \rangle$, representing the tension difference on the diagonal pairs of connected v-junctions, such that a positive value indicates higher tension on the upper right and lower left v-junctions and thus clockwise rotation (**Fig. 3F**, upper), and a negative value, the reverse (**Fig. 3F**, lower). We plotted $\Delta 1/\langle |U|^2 \rangle$ against the t-junction rotation rate and interestingly, and we found that 15 out of 16 data points from WT explants were in the first and third quadrants (**Fig. 3G**), consistent with our hypothesis illustrated in **Fig. 3F**. Linear correlational analysis also confirmed that the tension difference $\Delta 1/\langle |U|^2 \rangle$ was a stronger predictor of the t-junction rotation than was the overall tension (**Fig. 3G**, left vs. **Fig. S3B**, left). Strikingly, this correlation was also dependent upon Arvcf, as it was abolished in morphant cells (**Fig. 3H**). These data suggest that t-junction rotation is driven by differential high tension on diagonal pairs of connected v-junctions. With loss of Arvcf, t-junction rotation was restrained by both reduced v-junctional tension and by the loss of its correlation to the planar polarized tension difference.

Modeling suggests that cell packing configuration determines planar polarized force propagation.

We next asked how defects in t-junction rotation and the disruption of cell packing configuration (**Fig. 2&3**) is related to the failure of AP propagation of tissue-level CE after Arvcf loss (**Fig. 1**). We considered that v- and t-junctions are the main force bearing and generating elements in notochord tissue during CE. If we view them as quasi-static states analogous to beams and posts in a truss bridge, an optimal configuration will be needed to handle different loads. Thus, changes to cell packing configuration due to hindered t-junction rotation may have a direct impact on force distribution and force propagation in a tissue.

To test the effect of misaligned junctions within a cell sheet, we first examined *in silico* toy models with extreme cell packing configurations that exaggerated the features we observed in WT and Arvcf KD embryos. In the first model termed *Hexagon*, all cells were hexagonal and there is no AP-aligned t-junctions (**Fig. 4B**). In the second model termed *Brick-wall*, all cells were rectangular, so all t-junctions were AP-aligned (**Fig. 4C**). We then computationally applied high tension to a subset of specific v-junctions in the center of the tissue mimicking ML converging forces from cell intercalation (marked by asterisks in **Fig. 4B, C**), and used force balance-based cellular force inference technique illustrated in **Fig. 4A** (Brodland, et al., 2014) to ask how the force applied to those junctions would propagate across the tissue.

The difference was strikingly obvious, as indicated by the force heatmap in which junctions with warm colors carry more tension and those with cool colors carry less (index shown in **Fig. 4B**). In the *Hexagon* tissue, forces applied in the center (asterisks) propagated in both ML and AP directions so that junctions throughout the tissue carry high tensions (**Fig. 4B,** red/yellow). By contrast, applied forces in the *Brick-wall* tissue (**Fig. 4C**, asterisks) propagated only mediolaterally, forming two ML-aligned chains of high tension (**Fig. 4C**, red); both t and v-junctions above and below junctions with applied force displayed only low tensions (**Fig. 4C**, blue)

As a further test, we created a *Hybrid* tissue by embedding one AP-aligned t-junction in an otherwise hexagonal tissue (**Fig. 4D, d'**, hollow arrowhead). Forces applied in the middle of this hybrid tissue (asterisks) propagated in the ML direction and also towards the anterior (up) where there were no AP-aligned junctions (**Fig. 4D**). However, force propagation towards posterior (down) dropped immediately at the inserted AP-aligned t-junction (**Fig. 4d'**). These preliminary tests in toy models suggested that highly AP-aligned t-junctions can block AP force propagation.

Aberrant cell packing configuration disrupts planar polarized force propagation during CE *in vivo*.

Finally, we tested our force propagation model *in vivo* by assessing the distribution of forces in Keller explants. Using the same cellular force inference tool (Brodland, et al., 2014), we found that force distribution was heterogeneous across cells within WT explants, having regions with much higher tension and regions with lower tension (**Fig. 5A**). Interestingly, these regions of high tension spanned four to five cell diameters in both the AP and ML directions (**Fig. 5A**, diamonds; **Fig. 5C**, blue), suggesting a strong force coupling and force propagation in both AP and ML directions.

By contrast, the heterogenous force distribution in Arvcf KD explants displayed a distinctly different pattern. The high-tension regions were chain-like, extending only in the ML direction and not extending in the AP direction (**Fig. 5B; Fig. 5C**, orange). This pattern resembled the force propagation pattern in the *Brick-wall* toy model (**Fig. 4C**). Notably, there were a substantial number of AP-aligned t-junctions surrounding the high-tension region in Arvcf KD explant (**Fig. 5B**, hollow arrowheads). These data suggest that the excessive AP-aligned t-junctions resulting from the loss of Arvcf effectively block the propagation for forces from local cell intercalations, thus in turn further repressing v-junctional tension in the surrounding area.

Discussion

The overarching goal here was to explore the mechanisms by which microscale and macroscale behaviors are coordinated to achieve robust tissue scale morphogenesis. With that in mind, we combined live-imaging and image-based mechanical measurements across different scales and identified a multiscale linkage between ML cell intercalation behaviors and the AP propagation of forces during normal CE *in vivo*. Specifically, we show that strong planar polarized cellular forces are required, by rotating t-junctions away from the AP axis, for the final resolution of cell intercalation events (**Fig.3**). Such t-junction rotation is, in turn, critical, as failure to rotate results in aberrant cell packing, which limits force propagation specifically in the AP direction (**Fig. 4**, **Fig. 5A-C**). Thus, our data suggest a multiscale mechanical system, in which cellular forces for ML cell intercalation propagate along the AP axis to encourage cell intercalation events in the neighboring regions, thus propagating tissue-scale CE to maintain an efficient tissue morphogenesis (**Fig. 5D**).

This work provides important new insights into the role of nascent t-junctions, which by comparison to shortening v-junction remain only poorly studied, especially in vertebrates. In computational models such as vertex models, t-junction formation is a natural consequence after v-junction shortening is complete and is driven by polarized cortical tension and/or cell-cell adhesion (Bi, et al., 2015; Farhadifar, et al., 2007). *In vivo* studies of *Drosophila* germband CE have recognized the new t-junction extension as a direct contributor to tissue-level extension (Yu and Fernandez-Gonzalez, 2016), which at the cellular scale is driven by medial actomyosin pulses from the connected AP cells rather than the cortical actomyosin pulses (Yu and Fernandez-Gonzalez, 2016; Collinet, et al., 2015). Here, we have shown that in *Xenopus* notochord, the rate of new t-junction extension is not correlated with cortical tension on the connected v-junctions (**Fig. S3A**), which is similar to that in the *Drosophila* germband epithelium (Collinet, et al., 2015).

Importantly, our work here identified rotation as an important step following t-junction elongation that we show stems from planar polarized high tension in diagonal pairs of connected v-junctions (**Fig. 3**). In normal CE, cells display strong asynchronous actomyosin pulses on v-junctions (Huebner, et al., 2022; Shindo, et al., 2019), so that such a condition is easy to meet transiently to drive rapid t-junction rotation (**Fig. 2**). By contrast, both cortical tension and the amplitude of actomyosin pulses are significantly reduced after Arvcf depletion (**Fig. 3C**)(Huebner, et al., 2022), resulting in failure of T-junction rotation (**Fig. 3**). Arvcf depletion also dampens the pulsatile recruitment of cadherins to the v-junctions (Huebner, et al., 2022), which may also impact force transmission between cells. How this is related to the abolished correlation between t-junction rotation and the polarized tension difference (**Fig. 3H**) requires further investigation.

This subcellular defect in t-junction rotation then exerts a larger-scale defect by changing cell packing configuration, specifically by creating an excessive amount of AP-aligned t-junctions (**Fig.2**). Changes in cell packing and the associated biophysical properties are fundamental phenomena during morphogenesis (Lemke and Nelson, 2021; Petridou, et al., 2021; Wang, et al., 2020; Bi, et al., 2015). Although cell shape and cell density in the *Xenopus* notochord are significantly different from epithelia, in which cell packing configuration has been most studied, incorporating these ideas may provide some novel insight. Here, both modeling and experiment suggest that cell packing configuration significantly impacts force propagation in a planar polarized manner (**Fig. 4**, **Fig. 5A-C**). Interestingly, a recent vertex model of CE testing the effect of contraction timing, linked defective polarity of tension on v-junctions to not only cell packing defects (i.e. excess AP-aligned t-junctions), but also reduced cell intercalation and tissue-level CE (Shindo, et al., 2019). Therefore, t-junction rotation appears to be a key factor to maintain the packing configuration that favors force propagation and effective CE.

Finally, our data demonstrated the efficacy of our force assessment pipeline named Tension by Transverse Fluctuation (TFlux; see **Method**; **Fig. S2**). TFlux requires only cell membrane labeling and estimates junctional tension by tracking the transverse fluctuation of membranes along the interfaces of interest. This method is solely image-based, so that it is fully compatible with other live-imaging assays that also use a confocal or spinning disk microscopy. Because of its non-toxicity and non-invasiveness, it can be used to track tension on multiple cell interfaces over time. With further development, the method has the potential to achieve a spatial resolution of force close to the resolution of the microscope. This is appealing because cell-cell interfaces display very local heterogeneities during *Xenopus* notochord CE and other processes (Cavanaugh, et al., 2022; Weng, et al., 2022; Huebner, et al., 2021; Stephenson, et al., 2019). Thus, the broad accessibility, non-invasiveness, and the spatiotemporal resolution of the TFlux suggest it may have broad application for study cell biological and developmental processes.

To summarize, our data suggest that asynchronized high contraction force along the ML axis is required to tilt AP-aligned t-junctions to fully resolve individual cell intercalation events, such that ML aligned cellular forces can be coupled and propagated along the AP axis to propagate tissue level CE. This in turn forms a feed forward loop reinforcing both the cell behavior and tissue shape change.

Acknowledgements:

This work was supported by the NICHD (R01HD099191). We would also acknowledge Dr. Daniel J Dickinson for critical reading.

Author contributions

S.W. and J.B.W. conceptualized the project and wrote the manuscript. S.W. designed and conducted the experiments, performed analysis, and developed the model. R.J.H, and C.C.D assisted in data acquisition and analysis. S.W., B.M.N, and J.R.A. developed the TFlux. All authors provided revisions and comments.

Figure legend

Figure 1. CE propagation along the anteroposterior axis is required for embryonic axis elongation.

(A, B) Wildtype (A) and Arvcf KD (B) embryos at stage 11.5 and stage 14 as indicated, stained by *in situ* hybridization for the notochord-specific probe *Xnot*. Top panels show representative images of embryos. Bottom panels show stacked grayscale images of over 70 embryos for each condition. Dashed lines contour the average shape of the stained notochord with 50% coverage.

(C) Quantification of the normalized width difference between posterior and anterior ends of the notochords at stage 14. p values were calculated using Wilcoxon rank sum test (A.K.A. Mann-Whitney U test). $^{*}p < 0.05$; $^{**}p < 0.005$; $^{***}p < 0.0005$; NS, not significant.

(D, E) Convergent and extension of Wildtype (D) and Arvcf KD (E) explants during a two-hour incubation. Dashed lines mark a region of the notochord tissue at an equivalent stage of 13. Solid lines mark the same the region of the notochord tissue after a two-hour incubation. Two outlines were stacked together to show the convergence and extension of the explants (d' & e'). Black arrows mark the ML convergent of the notochord region at its anterior, middle, and posterior positions. Black hollow arrows mark the AP extension. Gray hollow arrowheads mark the regions with limited convergences.

(F) Schematic showing the quantification of explant shape change. Black hollow arrows mark the AP extension. Black arrows mark the ML convergence at the anterior, middle, and posterior of the notochord.

(G, H) Quantification of the AP extension (G) and ML convergence at the anterior, middle, and posterior ends of an explant (H). N = 24 for WT explants (blue) and N = 23 for Arvcf deficient explants (orange) from at least three replicates. p values were calculated using Wilcoxon rank sum test (A.K.A. Mann-Whitney U test). $^{*}p < 0.05$; $^{**}p < 0.005$; $^{***}p < 0.0005$; NS, not significant.

Figure 2. Loss of Arvcf changes tissue-wide cell packing configuration by slowing down the t-junction rotation.

(A) Schematic showing cell behaviors required for normal tissue-wide CE. Cells need to first elongate mediolaterally. After that, cells intercalate repeatedly in a polarized manner. The so-called v-junctions (light gray) linking anteroposterior neighboring cells shorten to bring mediolateral cells into contact, then t-junctions (dark gray) separating mediolateral cells form.

(B, C) Representative images of WT (B) and Arvcf KD (C) explants with membrane labeling showing the distinct cell packing configurations. Insets (b', c') are representative images showing the angle between t- and connected v-junctions ("tricellular angles"; solid lines). Hollow arrow heads mark the so-called AP aligned t-junctions that were perpendicular to the surrounding v-junctions.

(D) Distribution of the tricellular angle, defined as the smaller angle between t- and connected v-junctions for each cell (examples in b' and c'). Data points were pooled from 11 explants for each condition from at least three replicates and about 50 cells from each explant. p value was calculated using Kolmogorov–Smirnov test. $^{***}p < 0.0005$.

(E) Schematic showing the extension and rotation of a new t-junction formation.

(F, G) Still images from representative movies showing the formation of a new t-junction. Left panel, t-junctions start to form when the ML cells meet. Middle panels, t-junctions extend along the AP axis. Right panels, t-junctions rotate suddenly at the end of the extension phase.

(H-J) Quantification of the dynamics of a t-junction formation. The extension time (H), extension rate (I), and the rotation rate (J) were compared between WT and Arvcf KD explants. N = 32 for t-junctions from WT explants and N = 26 from Arvcf KD explants. Explants were collected from at least three replicates. p values were calculated using Wilcoxon rank sum test (A.K.A. Mann-Whitney U test). $^{**}p < 0.005$; $^{***}p < 0.0005$.

Figure 3. T-junction rotation requires differential high tension on the connected v-junctions.

(A) Schematic illustrating that transverse fluctuation of a junction is inversely correlated with its junctional tension. High junctional tension correlates with low transverse fluctuation, and vice versa. See **Method** and **Fig. S2** for the details.

(B, C) Quantification of tension on the v- and t-junctions in WT and Arvcf KD explants. (B) Representative junctions of interest were highlighted. (C) The reciprocal of the mean square transverse fluctuation (i.e., “$1/\langle|U|^2\rangle$”) was used as a force index to compare tension on v- and t-junctions. N = 19, 28, 31, 40 from left to right, pooled from at least three replicates. p values were calculated using Wilcoxon rank sum test (A.K.A. Mann-Whitney U test). $^{**}p < 0.005$; $^{***}p < 0.0005$.

(D, E) Representative images showing the dynamics of a t-junction rotation and tension analysis on the connected v-junctions. Transverse fluctuation, U, on the adjacent 10-μm region of each connected v-junctions during the first 5-min of the t-junction formation was measured (D). The force index, $1/\langle|U|^2\rangle$, was quantified and displayed in a color-coded manner as an overlay on top of the junction image (E).

(F) Schematic showing that planar polarized tension on diagonal v-junctions directs the connected t-junction rotation. Top panel, a t-junctions rotates clockwise when tensions on the upper right and lower left v-junctions are higher than tensions on the other diagonal pair. Bottom panel, a t-junction rotates anticlockwise when tensions on the upper left and lower right v-junctions are higher.

(G, H) Plot showing the t-junction rotation rate verses the difference of the force index on the diagonal pairs of v-junctions ($\Delta 1/\langle|U|^2\rangle$). A positive value of $\Delta 1/\langle|U|^2\rangle$ indicates higher tension on the upper right and lower left v-junctions and a vice versa. Cross markers represent data points, solid lines are linear fitting, and dashed lines are upper and lowers boundaries with 95% confidence. N = 16 for both WT and KD conditions.

Figure 4. Modeling of cell packing configuration and planar polarized force propagation.

(A) Schematic showings the basic principles of the cellular force interference technique, i.e. force balance at each tricellular vertex.

(B-D) Force propagation simulated using cellular force inference in toy models with different cell packing. A *Hexagon* model (B) has all cells hexagonal and no AP-aligned t-junctions. A *Brick-wall* model (C) has all cell rectangle and all t-junctions AP-aligned. A *Hybrid* model (D) has one AP-aligned t-junction (white hollow arrowhead) embedded in an otherwise *Hexagon* model. Forces mimicking the ML converging force from cell intercalation event were applied on the v-junctions marked with asterisks in the center of a toy model tissue and force distribution in the rest of the tissue was estimated. Force on each junction is indicated by the color.

Figure 5. Aberrant cell packing configuration disrupts polarized force propagation and thus blocks CE propagation.

(A, B) Force distribution estimated using the cellular force inference in WT (A) and Arvcf KD (B) explants. v-junctions with the maximum force (dark red) and their adjacent v-junctions with forces greater than the average (warm color) are marked with diamonds. Hollow arrowheads mark the t-junctions perpendicular to the apposed v-junctions.

(C) Quantification of force coupling in the AP and ML directions in WT and Arvcf KD explants. Number of adjacent cells having forces on v-junctions above average were quantified as the number of cells with force coupled. Data pooled from 20 WT explants and 17 Arvcf KD explants from at least three replicates. p values were calculated using Wilcoxon rank sum test (A.K.A. Mann-Whitney U test). ***$p < 0.0005$; NS, not significant.

(D) Multiscale biomechanical model underpinning tissue-scale CE propagation. Asynchronized higher planar polarized tension (WT condition) rotates the t-junctions, so that forces from local convergence (asterisks) propagate in the AP direction, favoring the propagation of CE also in the AP direction. Lower tension (Arvcf KD condition) slows down the t-junction rotation, maintaining the cell packing configuration that can effectively block force propagation in the AP direction, thus blocked CE propagation.

Supplementary figure legend

Figure S1. Loss of Arvcf does not change ML cell elongation.

(A) Quantification of the length-to-width ratio of WT and Arvcf KD cells in explants. N = 43 for WT and KD cells from at least three replicates. p values were calculated using Wilcoxon rank sum test (A.K.A. Mann-Whitney U test). NS, not significant, $p>0.05$.

Figure S2. Tension by transverse fluctuation (TFlux).

(A) Tracking of a cell-cell interface over time displayed in the 3D xyt coordinates. Rough edges on the left and right sides of the 3D surface show overall movement of the interface over time. Lightening is added to show the roughness of the surface.

(B) Tracking of the smoothed cell-cell interface over time displayed in the 3D xyt coordinates. At each time point, a moving average of 2 μm along the length of the interface is performed. Same lightening is added to show that the surface is smoothened.

(C) The “baseline” surface displayed in the 3D xyt coordinates. A moving average of 20 sec is performed on the smoothed surface in (B) to capture only the low-frequency overall movement of the interface in the x-y plane.

(D) Transverse fluctuation (U, gray arrows) is defined as the distance between the original position of the interface as in (A) (solid line) to the baseline position quantified in (C) (dashed line).

(E) Kymograph showing the spatiotemporal pattern of the transverse fluctuation, U. Force index $1/\langle|U|^2\rangle$ is the reciprocal of the mean transverse fluctuation over the entire interface in a 5-min duration of observation.

Figure S3. T-junction extension and rotation are not correlated with the average tension on the connected v-junctions.

(A) Plot showing the t-junction extension rate verses the average of the force index $1/\langle|U|^2\rangle$ on four connected v-junctions. Cross markers represent data points, solid lines are linear fitting, and dashed lines are upper and lowers boundaries with 95% confidence. N = 16 for both WT and KD conditions.

(B) Plot showing the t-junction rotation rate verses the average of the force index $1/\langle|U|^2\rangle$ on four connected v-junctions. Cross markers represent data points, solid lines are linear fitting, and dashed lines are upper and lowers boundaries with 95% confidence. N = 16 for both WT and KD conditions.

Methods:

Xenopus embryo manipulations

Ovulation was induced by injecting adult female Xenopus laevis with 600 units of human chorionic gonadotropin (HCG, MERCK Animal Health) and animals were kept at 16 dc overnight. Eggs were acquired the following day by squeezing the ovulating females and eggs were fertilized *in vitro*. Eggs were dejellied in 2.5% cysteine (pH 7.9) 1.5 hours after fertilization and reared in 1/3x Marc's modified Ringer's (MMR) solution. For micro-injection, embryos were placed in 2% ficoll in 1/3x MMR during injection and washed in 1/3x MMR 30 min after injection. Embryos were injected in the dorsal blastomeres at the 4-cell stage targeting the C1 cell at 32-cell stage and presumptive notochord. Keller explants were dissected at stage 10.25 in Steinberg's solution using hair tools.

Plasmids and Morpholinos

The Arvcf morpholino has been previously described (5'-ACACTGGCAGACCTGAGCCTATGGC-3' (Fang, et al., 2004) and was ordered from Gene Tools, LLC. Membrane-BFP plasmid was made in pCS2.

mRNA and morpholino microinjections

Capped mRNAs were generated using the ThermoFisher SP6 mMessage mMachine kit (Catalog number: AM1340). Membrane-BFP mRNAs were injected at 75 pg per blastomere.

In situ hybridization

Whole-mount *in situ* hybridization was performed as descried previously using a DIG-labeled single-strand RNA probe against a partial sequence of *Xnot (Monsoro-Burq, 2007; Sive, et al., 2000)*. This antisense probe has been well characterized, which shows *Xnot* expression in the prenotochordal region about the dorsal lip at stage 10.5 and along the dorsal midline exclusive to the notochord up to stage 16 (von Dassow, et al., 1993). Bright field images were captured with a Zeiss Axio Zoom. V16 stereo microscope with Carl Zeiss Axiocam HRc color microscope camera or a Leica stereo microscope MDG41 with AmScope microscope digital camera WF200.

Imaging *Xenopus* explants

Explants were submerged in Steinberg's solutions and cultured on glass coverslips coated with Fibronectin (Sigma-Aldrich, F1141) at 5 µg/cm^2. All images of membrane labeling (Membrane-BFP) were taken on a Nikon A1R, and at the focal plane 5 µm deep into the explant. For tracking tissue-scale CE, the first image was taken after a 3-hour incubation at room temperature. A second image was taken another two hours later. All other assays were started after a 5-hour incubation of the explant. For tracking the dynamic of t-junction formation, we set the standard confocal time-lapse imaging at an interval of 5 sec. For the force inference by transverse fluctuation, we set the time interval of 1 sec.

Tension by Transverse Fluctuation (TFlux)

The transverse fluctuation of a junction is inversely proportional to tension on the junction (**Fig. 3A**). Based on this basic idea, we developed an image-based non-invasive force assessment method named Tension by Transverse Fluctuation ("TFlux"). Membrane labeling is required to track the position of a junction over time. We labeled the membrane by injecting embryos at the 4-cell stage in both dorsal blastomeres with Mem-BFP mRNA. Keller explants were then dissected from early gastrula embryos, mounted on fibronectin coated coverslips, incubated in the Steinberg's solution at room temperature for five hours, and then live-imaged on a Nikon A1R confocal microscope for 5 min. To capture small transverse fluctuations along a junction, high spatiotemporal resolution is required. We used time interval of 1 sec and pixel size of 0.20 µm.

To measure the transverse fluctuations, time-lapse movies were imported into Ilastik® and apposing cells were first segmented using Ilastik® pixel classification and Ilastik® Carving. 3D (xyt) meshes of the two cells were then imported to a customized MATLAB script to detect the interface over time (**Fig. S2A**). We then defined a base-line position of the junction at each time point to account for the overall movement of the cells and the junction. To do so, we performed a moving average over 2 *µ*m along the junction length at each time point (**Fig. S2B**), and then another moving average over 20 sec (**Fig. S2C**). Transverse fluctuation was then measure at each time point as the distance from the original junction position to the base line (**Fig. S2D**, **E**). The overall junction tension, referred to as the force index, is defined as the reciprocal of the mean square transverse fluctuation of the entire junction of interest over the 5-min of observation.

References:

Abuwarda, H., and Pathak, M.M. (2020). Mechanobiology of neural development. Curr Opin Cell Biol 66, 104-111.
Alvarado, J., and Koenderink, G.H. (2014). Active Mechanics of the Cytoskel.
Arslan, F.N., Eckert, J., Schmidt, T., and Heisenberg, C.-P. (2021). Holding it together: when cadherin meets cadherin. Biophysical Journal.
Bi, D., Lopez, J.H., Schwarz, J.M., and Manning, M.L. (2015). A density-independent rigidity transition in biological tissues. Nature Physics 11, 1074.
Brodland, G.W., Veldhuis, J.H., Kim, S., Perrone, M., Mashburn, D., and Hutson, M.S. (2014). CellFIT: A Cellular Force-Inference Toolkit Using Curvilinear Cell Boundaries. PLOS ONE 9, e99116.
Butler, M.T., and Wallingford, J.B. (2017). Planar cell polarity in development and disease. Nature Reviews Molecular Cell Biology 18, 375-388.
Cavanaugh, K.E., Staddon, M.F., Chmiel, T.A., Harmon, R., Budnar, S., Yap, A.S., Banerjee, S., and Gardel, M.L. (2022). Force-dependent intercellular adhesion strengthening underlies asymmetric adherens junction contraction. Current Biology 32, 1986-2000.e5.
Collinet, C., Rauzi, M., Lenne, P.F., and Lecuit, T. (2015). Local and tissue-scale forces drive oriented junction growth during tissue extension. Nat Cell Biol 17, 1247-58.
Fang, X., Ji, H., Kim, S.-W., Park, J.-I., Vaught, T.G., Anastasiadis, P.Z., Ciesiolka, M., and McCrea, P.D. (2004). Vertebrate development requires ARVCF and p120 catenins and their interplay with RhoA and Rac. The Journal of Cell Biology 165, 87-98.
Farhadifar, R., Roper, J.C., Aigouy, B., Eaton, S., and Julicher, F. (2007). The influence of cell mechanics, cell-cell interactions, and proliferation on epithelial packing. Curr Biol 17, 2095-104.
Goodwin, K., and Nelson, C.M. (2021). Mechanics of Development. Dev Cell 56, 240-250.
Hara, Y., Nagayama, K., Yamamoto, T.S., Matsumoto, T., Suzuki, M., and Ueno, N. (2013). Directional migration of leading-edge mesoderm generates physical forces: Implication in Xenopus notochord formation during gastrulation. Developmental Biology 382, 482-495.
Huebner, R.J., Malmi-Kakkada, A.N., Sarıkaya, S., Weng, S., Thirumalai, D., and Wallingford, J.B. (2021). Mechanical heterogeneity along single cell-cell junctions is driven by lateral clustering of cadherins during vertebrate axis elongation. eLife 10, e65390.
Huebner, R.J., Weng, S., Lee, C., Sarıkaya, S., Papoulas, O., Cox, R.M., Marcotte, E.M., and Wallingford, J.B. (2022). ARVCF catenin controls force production during vertebrate convergent extension. Developmental Cell.
Keller, R. (2002). Shaping the vertebrate body plan by polarized embryonic cell movements. Science 298, 1950-4.
Kidokoro, H., Yonei-Tamura, S., Tamura, K., Schoenwolf, G.C., and Saijoh, Y. (2018). The heart tube forms and elongates through dynamic cell rearrangement coordinated with foregut extension. Development 145, dev152488.
Ladoux, B., and Mege, R.M. (2017). Mechanobiology of collective cell behaviours. Nat Rev Mol Cell Biol 18, 743-757.
Lemke, S.B., and Nelson, C.M. (2021). Dynamic changes in epithelial cell packing during tissue morphogenesis. Current Biology 31, R1098-R1110.
Levayer, R., and Lecuit, T. (2013). Oscillation and polarity of E-cadherin asymmetries control actomyosin flow patterns during morphogenesis. Dev Cell 26, 162-75.
Lienkamp, S.S., Liu, K., Karner, C.M., Carroll, T.J., Ronneberger, O., Wallingford, J.B., and Walz, G. (2012). Vertebrate kidney tubules elongate using a planar cell polarity-dependent, rosette-based mechanism of convergent extension. Nat Genet 44, 1382-7.
Maroudas-Sacks, Y., and Keren, K. (2021). Mechanical Patterning in Animal Morphogenesis. Annu Rev Cell Dev Biol 37, 469-493.
Monsoro-Burq, A.H. (2007). A rapid protocol for whole-mount in situ hybridization on Xenopus embryos. CSH Protoc 2007, pdb prot4809.

Niessen, C.M., Leckband, D., and Yap, A.S. (2011). Tissue organization by cadherin adhesion molecules: dynamic molecular and cellular mechanisms of morphogenetic regulation. Physiol Rev 91, 691-731.
Pannekoek, W.J., de Rooij, J., and Gloerich, M. (2019). Force transduction by cadherin adhesions in morphogenesis. F1000Res 8.
Paulson, A.F., Mooney, E., Fang, X., Ji, H., and McCrea, P.D. (2000). Xarvcf, Xenopus Member of the p120 Catenin Subfamily Associating with Cadherin Juxtamembrane Region *. Journal of Biological Chemistry 275, 30124-30131.
Petridou, N.I., Corominas-Murtra, B., Heisenberg, C.P., and Hannezo, E. (2021). Rigidity percolation uncovers a structural basis for embryonic tissue phase transitions. Cell 184, 1914-1928 e19.
Shih, J., and Keller, R. (1992). Patterns of cell motility in the organizer and dorsal mesoderm of Xenopus laevis. Development 116, 915-30.
Shindo, A. (2018). Models of convergent extension during morphogenesis. Wiley Interdisciplinary Reviews: Developmental Biology 7, e293.
Shindo, A., Inoue, Y., Kinoshita, M., and Wallingford, J.B. (2019). PCP-dependent transcellular regulation of actomyosin oscillation facilitates convergent extension of vertebrate tissue. Developmental Biology 446, 159-167.
Shindo, A., and Wallingford, J.B. (2014). PCP and septins compartmentalize cortical actomyosin to direct collective cell movement. Science 343, 649-52.
Sive, H.L., Grainger, R.M., and Harland, R.M. (2000). Early development of Xenopus laevis: a laboratory manual CSHL Press)
Stephenson, R.E., Higashi, T., Erofeev, I.S., Arnold, T.R., Leda, M., Goryachev, A.B., and Miller, A.L. (2019). Rho Flares Repair Local Tight Junction Leaks. Developmental Cell 48, 445-459.e5.
Sutherland, A., Keller, R., and Lesko, A. (2020). Convergent extension in mammalian morphogenesis. Semin Cell Dev Biol 100, 199-211.
Tada, M., and Heisenberg, C.P. (2012). Convergent extension: using collective cell migration and cell intercalation to shape embryos. Development 139, 3897-904.
von Dassow, G., Schmidt, J.E., and Kimelman, D. (1993). Induction of the Xenopus organizer: expression and regulation of Xnot, a novel FGF and activin-regulated homeo box gene. Genes Dev 7, 355-66.
Wallingford, J.B., Niswander, L.A., Shaw, G.M., and Finnell, R.H. (2013). The continuing challenge of understanding, preventing, and treating neural tube defects. Science 339, 1222002.
Wang, X., Merkel, M., Sutter, L.B., Erdemci-Tandogan, G., Manning, M.L., and Kasza, K.E. (2020). Anisotropy links cell shapes to tissue flow during convergent extension. Proc Natl Acad Sci U S A 117, 13541-13551.
Weng, S., Huebner, R.J., and Wallingford, J.B. (2022). Convergent extension requires adhesion-dependent biomechanical integration of cell crawling and junction contraction. Cell Reports 39.
Yu, J.C., and Fernandez-Gonzalez, R. (2016). Local mechanical forces promote polarized junctional assembly and axis elongation in Drosophila. eLife 5, e10757.
Zhou, J., Kim, H.Y., and Davidson, L.A. (2009). Actomyosin stiffens the vertebrate embryo during crucial stages of elongation and neural tube closure. Development 136, 677-88.

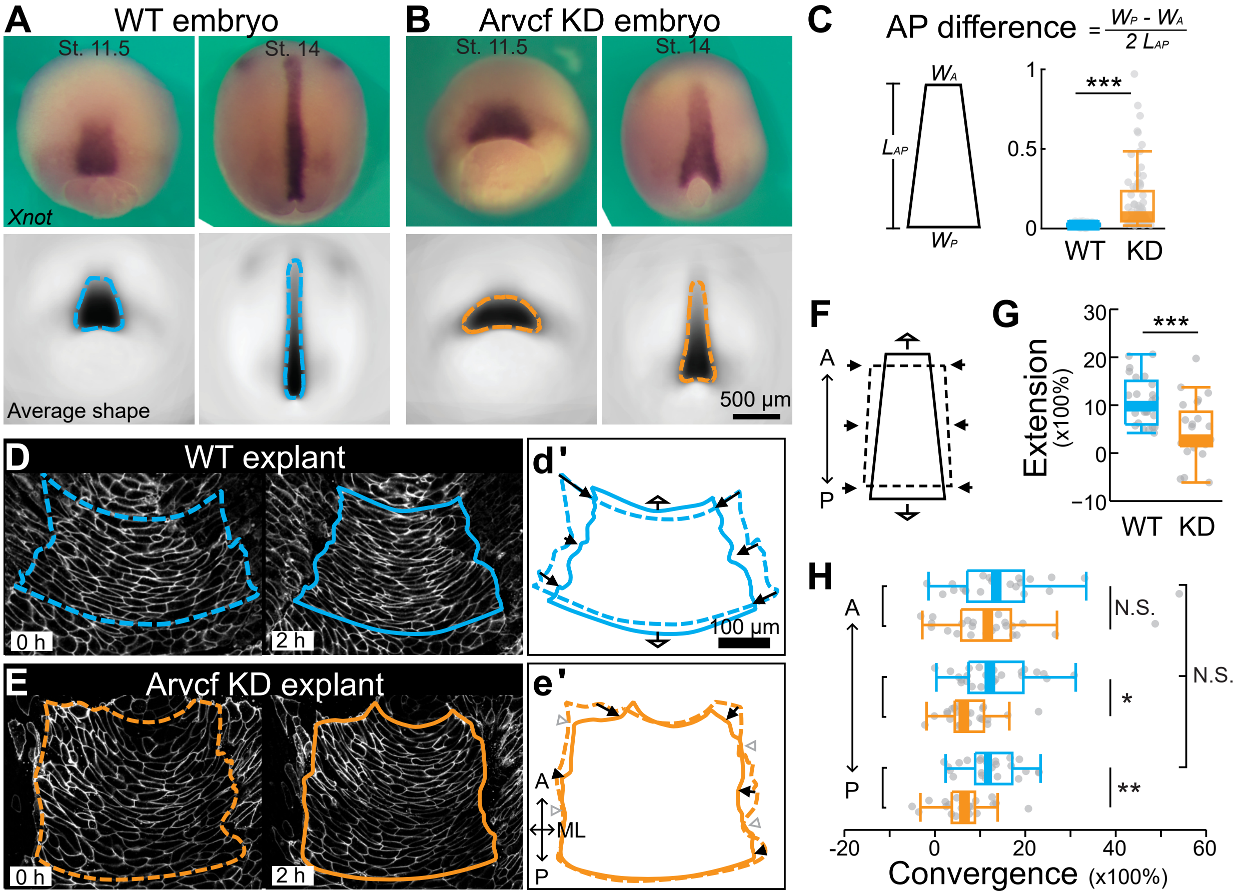

Weng et al. Figure 1

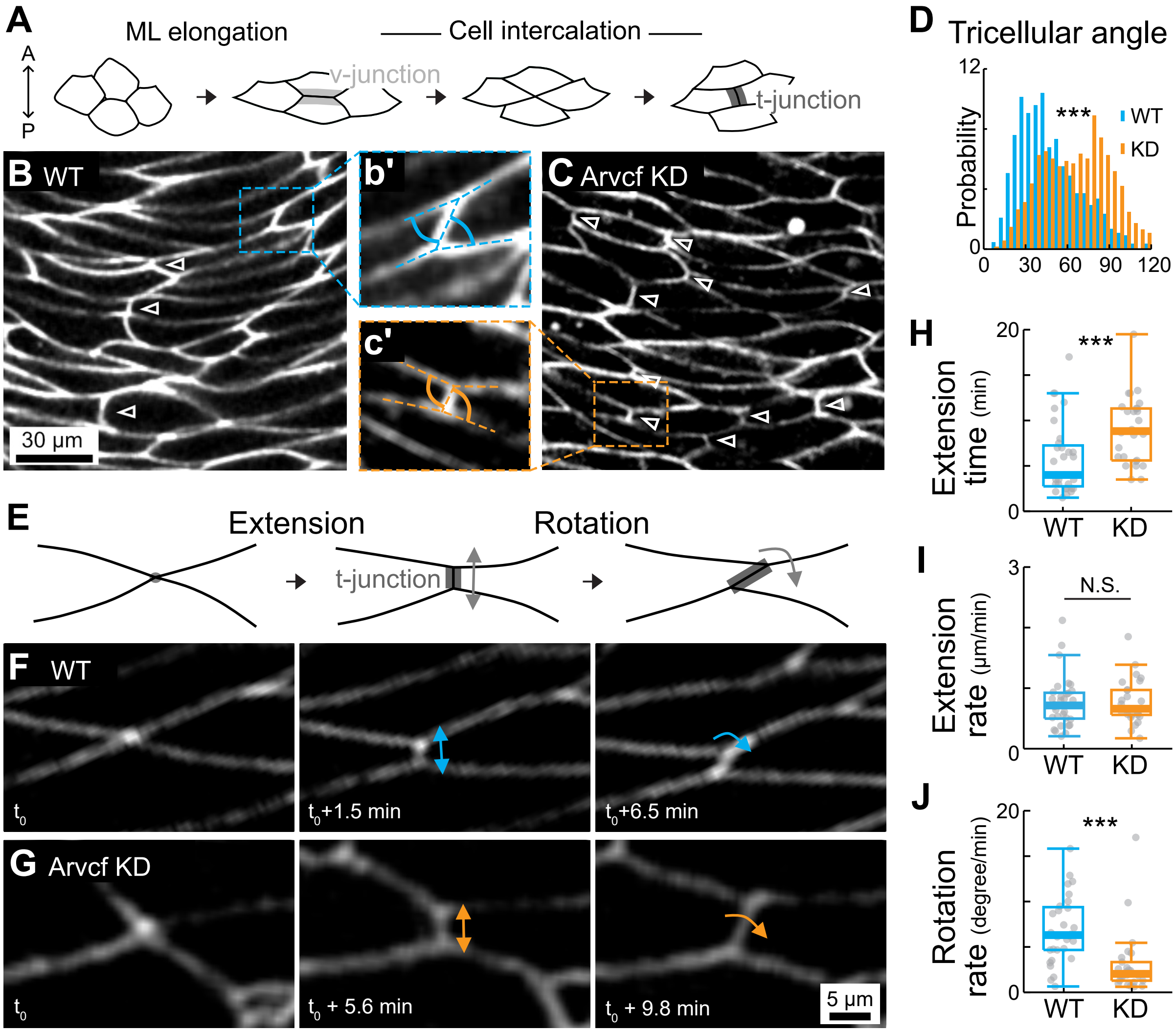
A
ML elongation
Cell intercalation
A
P
v-junction
t-junction
B WT
30 μm
b'
c'
C Arvcf KD
D Tricellular angle
Probability
12
0
0
30
60
90
120
***
WT
KD
H
Extension time (min)
20
0
***
WT
KD
I
Extension rate (μm/min)
3
0
N.S.
WT
KD
J
Rotation rate (degree/min)
20
0
***
WT
KD
E
Extension
Rotation
t-junction
F WT
t_0
t_0+1.5 min
t_0+6.5 min
G Arvcf KD
t_0
t_0 + 5.6 min
t_0 + 9.8 min
5 μm

Weng et al. Figure 2

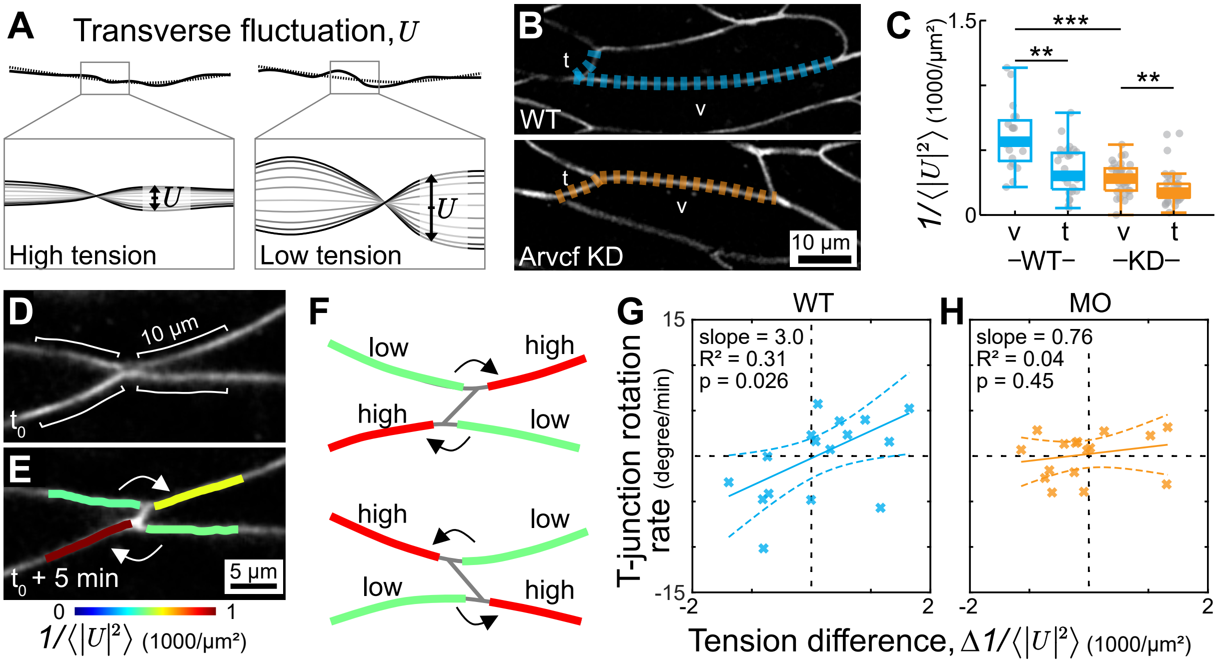

Weng et al. Figure 3

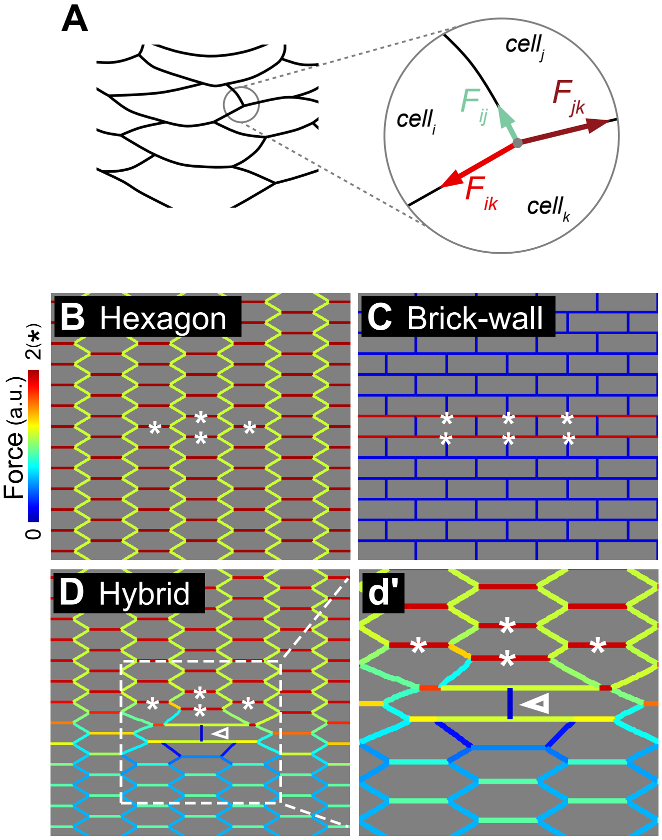
A
cell_j
F_ij
F_jk
cell_i
F_ik
cell_k
B Hexagon
C Brick-wall
Force (a.u.)
0
2(*)
D Hybrid
d'

Weng et al. Figure 4

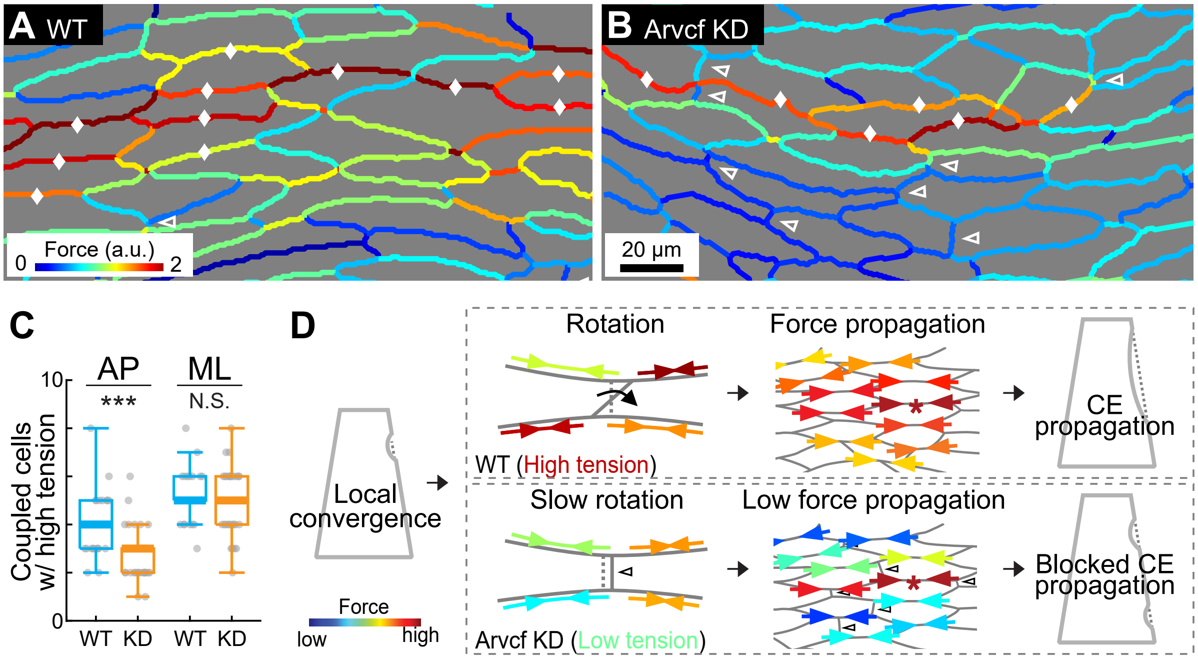

Weng et al. Figure 5

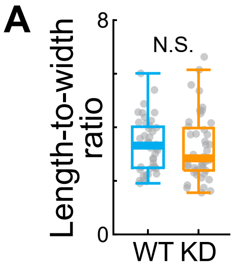

Weng et al. Figure S1

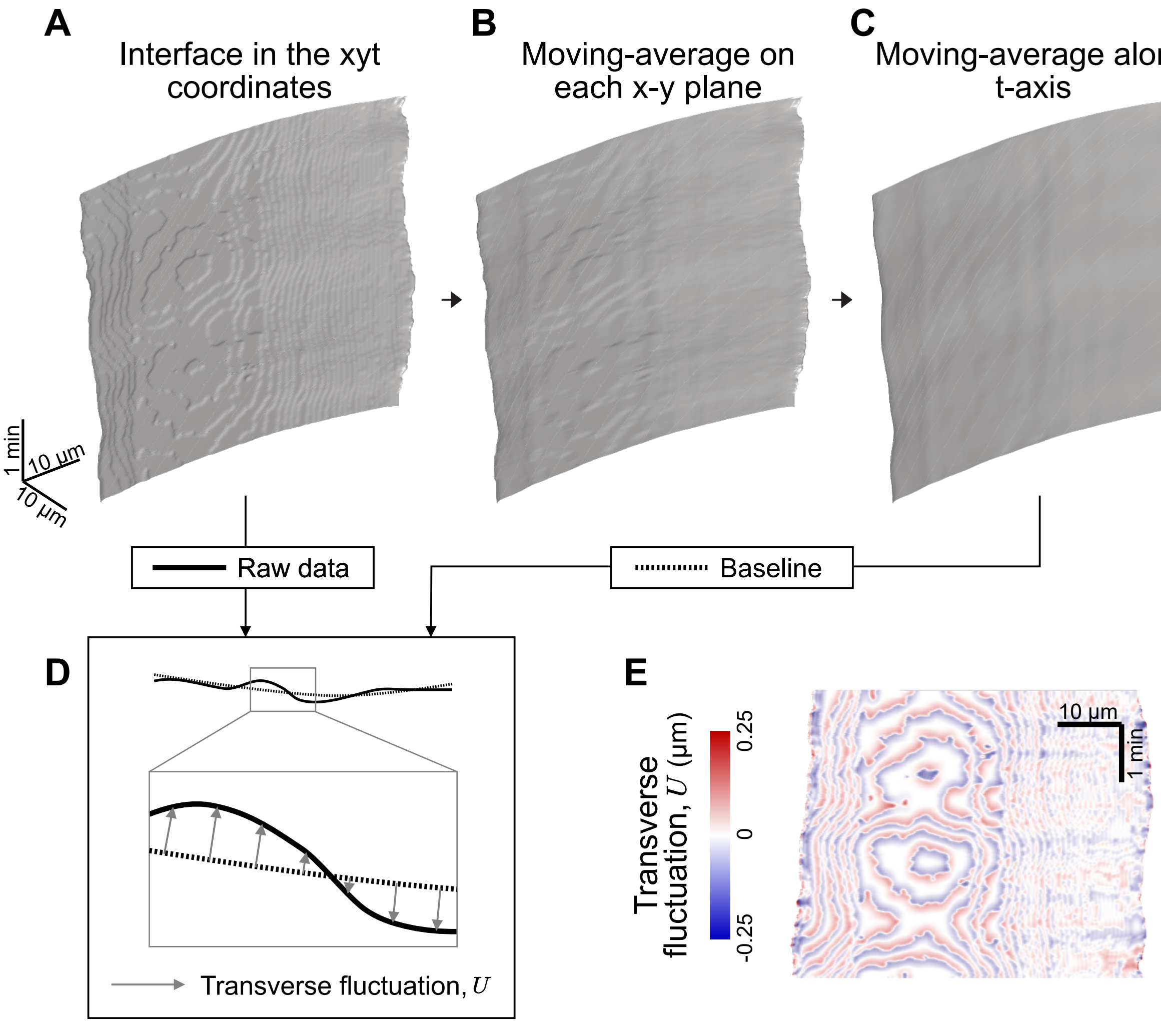
A
Interface in the xyt coordinates
B
Moving-average on each x-y plane
C
Moving-average along t-axis
1 min
10 μm
10 μm
Raw data
Baseline
D
Transverse fluctuation, U
E
Transverse fluctuation, U (μm)
0.25
0
-0.25
10 μm
1 min

Weng et al. Figure S2

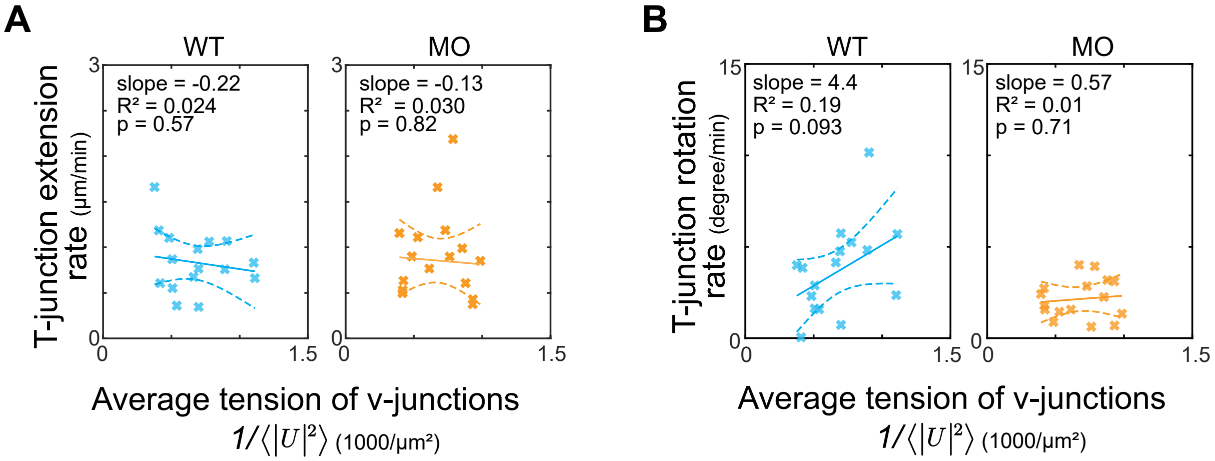

Weng et al. Figure S3